Appl Phys A (2009) 94: 999–1009
DOI 10.1007/s00339-008-4885-4

Applied Physics A
Materials Science & Processing

Femtosecond laser ablation characteristics of nickel-based superalloy C263

N.G. Semaltianos · W. Perrie · P. French · M. Sharp · G. Dearden · S. Logothetidis · K.G. Watkins

Received: 12 May 2008 / Accepted: 25 August 2008 / Published online: 20 September 2008

Abstract Femtosecond laser (180 fs, 775 nm, 1 kHz) ablation characteristics of the nickel-based superalloy C263 are investigated. The single pulse ablation threshold is measured to be 0.26 ± 0.03 J/cm^2 and the incubation parameter $\xi = 0.72 \pm 0.03$ by also measuring the dependence of ablation threshold on the number of laser pulses. The ablation rate exhibits two logarithmic dependencies on fluence corresponding to ablation determined by the optical penetration depth at fluences below $\sim$5 J/cm^2 (for single pulse) and by the electron thermal diffusion length above that fluence. The central surface morphology of ablated craters (dimples) with laser fluence and number of laser pulses shows the development of several kinds of periodic structures (ripples) with different periodicities as well as the formation of resolidified material and holes at the centre of the ablated crater at high fluences. The debris produced during ablation consists of crystalline C263 oxidized nanoparticles with diameters of $\sim$2–20 nm (for $F = 9.6$ J/cm^2). The mechanisms involved in femtosecond laser microprocessing of the superalloy C263 as well as in the synthesis of C263 nanoparticles are elucidated and discussed in terms of the properties of the material.

PACS 79.20.Ds · 81.05.Bx · 68.37.Hk · 68.37.Ps · 81.07.-b

N.G. Semaltianos (✉) · W. Perrie · P. French · M. Sharp · G. Dearden · K.G. Watkins
Department of Engineering, University of Liverpool, Brownlow Hill, Liverpool L69 3GH, UK
e-mail: n.semaltianos@liverpool.ac.uk

S. Logothetidis
Department of Physics, Aristotle University of Thessaloniki, Thessaloniki 54124, Greece

1 Introduction

Nickel-based superalloys are commonly used in the aerospace industry for the manufacturing of aero-engine components. They contain a large number of chemical elements and can be divided into two main groups: one in which the alloys contain 'heavy metals' Ta, W and Re (which give to the material high temperature solution strength) and also low concentration of magnetic elements and another one in which the alloys contain high percentage of elements found in the same period of the periodic table as Ni, such as Cr, Co, Mn and Fe. The solid solution is strengthened by those elements as well as by Mo.

Micromachining of aero-engine components made out of nickel-based superalloys and which are subjected to high thermal loading during in-service operating conditions is often carried out for the manufacturing of cooling holes. This is done industrially, by laser processing and in particular using either lamp pumped or Diode Pumped Solid State (DPSS) Nd:YAG laser systems (pulse widths: 0.5–1.0 ms, pulse energies: 5–18 J) due mainly to the fact that, because of their high average power, these lasers result in high throughput [1]. In addition to cooling holes, the presence of other surface features such as dimples on aero-engine parts is also important as such features in combination with cooling holes could assist in an increase of the thickness of the air boundary layer on the surface of the relevant part or even in the conversion of the boundary layer flow from laminar to turbulent thus offering novel cooling geometries with improved thermal-hydraulic performance [2–4]. The tribological properties of mechanical components can also be enhanced by the presence of such surface features [5].

Early investigation of laser ablation of nickel-based alloys included excimer laser machining (wavelength (λ) = 248 nm, fluence (F) = 0.68–10.20 kJ/cm^2, pulse width:

33 ns, frequency (f) = 10, 50, 100 Hz, number of pulses (N) = 100, 200, 500 or 1000) of the superalloy CMSX-2 [6] and especially the determination of the relationship between the laser parameters (F, f and N) and the shape of the formed ablated craters, the proportion of the ablated material and the laser hardening effects. For the highest energy density applied (10.2 kJ/cm^2), the formed craters were shown to be cone-shaped. The metallurgical reactions such as resolidification of the recast layer found in the laser machined residual surface of the superalloys: Inconel 718, Waspaloy and IN-713 as well as the role of carbides were investigated and elemental maps of cross sections through the recast layer were presented [7].

Although long pulse width lasers used in machining of superalloys result in a high throughput (due to their high average power), they also result however, in the formation of a number of processing-induced defects on the machined features (caused by the resolidification of the ejected melted material), microcracks in the heat affected zone (HAZ) and damage in the adjacent structures caused by the formation of surface shock waves, and these defects adversely affect the fatigue time of the relevant part, also resulting in an increase of the cost and of the post-processing time for their elimination [8].

Lately, femtosecond lasers have been introduced as a powerful "tool" for the microprocessing of many different materials [9], avoiding the formation of many undesirable defects caused by the laser processing of the material. This is mainly due to the fact that because the pulse width is shorter than the time it takes for the electrons to transfer their energy to the lattice (due to the electron–phonon coupling), there is no dissipation of laser beam energy out of the irradiation spot into heat during absorption of the energy by the electrons, and this results in a direct solid to vapour transition even at low pulse energies [10]. The ultrashort pulse width also allows the achievement of very high peak laser intensity with relatively low pulse energy. These characteristics result in precisely defined ablation thresholds, reduction of the HAZ and increase of the efficiency of the ablation process but with a sacrifice of the throughput rate due to the low average power involved [11].

Although there are a number of reports in the literature on femtosecond laser ablation of pure metals, data and systematic investigations on femtosecond laser ablation characteristics of superalloys are still very limited. The superiority of using femtosecond laser pulses (780 nm, 150 fs, 1 kHz) for machining holes and trenches in single crystal superalloys was demonstrated in MK-4 (superalloy of the first group), and the single pulse ablation threshold was measured to be 332 ± 14 mJ/cm^2 ($w_0 = 28.4$ μm) [12]. This was also demonstrated in Thermal Barrier Coated (TBC) superalloys René N5 and CMSX-4 [13] (also of the first group of superalloys). The two different ablation regimes corresponding to ablation determined by the optical penetration depth at low fluences and the electron thermal diffusion length at high fluences (which are characteristic of the laser ablation of materials using ultrashort pulses) were measured in the femtosecond laser ablation of CMSX-4 (780 nm, 150 fs, 125 Hz). The single pulse ablation threshold was measured to be 0.30 ± 0.03 J/cm^2 ($w_0 = 34.6$ μm) [14] and the incubation factor $\xi = 0.86 \pm 0.03$ [15]. The surface morphology of the ablated craters was characterised by ripples in the low fluences region, while in the high fluences region, resolidified regions were observed around the perimeter, on the sidewalls or on the bottom of the ablated holes but still no porosity, cracks or precipitate coarsening was observed.

This paper involves a systematic investigation of femtosecond laser ablation characteristics of the nickel-based superalloy C263 (superalloy of the second group). We report measurements and their comparison with results already reported in the literature for other superalloys, of important parameters which control femtosecond laser ablation of the superalloy C263. In particular, the single pulse ablation threshold of the material was determined, and the ablation threshold dependence on the number of laser pulses used for ablation was investigated in detail as well as the role of the incubation effect in the ablation process. The morphological and microstructural characteristics of the debris nanoparticles which are produced during femtosecond laser ablation of the material, the dependence on laser fluence of the ablation rate corresponding to single pulse but also to multipulse ablation of the material and the determination of the two ablation regimes at low and high fluences is presented. The results and findings reported in the paper are important in the field of femtosecond laser ablation and surface modification of superalloys.

2 Experimental details

A Clark-MXR 2010 turnkey femtosecond laser system based on chirped pulse amplification [16] was used for superalloy laser ablation studies. A mode locked, diode pumped Erbium doped ring fibre laser at 1550 nm whose output is frequency doubled to 775 nm in periodically poled lithium niobate is used to seed a Ti–sapphire regenerative amplifier. The laser system delivers ∼1 mJ per pulse at 1 kHz repetition rate and $\lambda = 775$ nm, 180 fs pulse length and observed bandwidth $\Delta\lambda \sim 5.5$ nm. Beam intensity spatial profile is near Gaussian with a measured 3D Gaussian fit parameter of ∼0.87. The enclosure temperature is stabilised at 20 °C using a small dedicated chiller which also keeps the Ti–sapphire crystal temperature stable. Output pulse stability is typically ±1% (1s), while prepulse and post-pulse amplitudes were minimised and measured to be <0.2 and 1.7%, respectively.

Figure 1 shows a diagram of the experimental set-up. The output from the Clark-MXR 2010 laser system passed

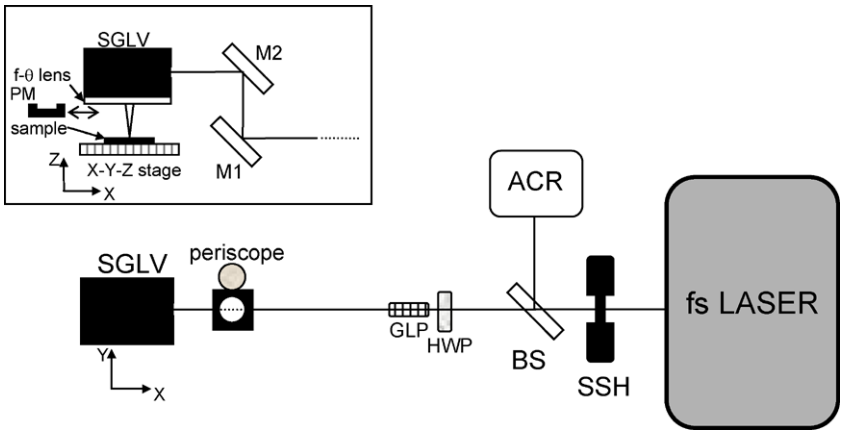

Fig. 1 Schematic diagram of the experimental setup. SSH: safety shutter, BS: beam splitter, ACR: auto-correlator, M1, M2: mirrors, HWP: $\lambda/2$ plate, GLP: Glan laser polariser, SGLV: scanning galvanometer, PM: power meter

Table 1 Elemental composition (%wt) of superalloy C263

	O	C	Si	Cu	Fe	Mn	Cr	Ti	Al	Co	Mo	Zr	B	S	Ni
Ref. [17]	–	0.03	0.25	0.20 max	0.75 max	0.40	20.0	2.15	0.45	20.0	5.9	0.02 max	0.001 max	0.007 max	bal.
This work	3.7	–	0.2	0.0	0.6	0.8	19.8	2.0	0.3	18.4	5.4	0.3	0.0	1.9	46.7

through a laser safety shutter (SSH), a pick-off beam splitter (BS) for auto-correlation and then through an attenuator ($\lambda/2$ plate (HWP) and Glan laser polariser (GLP)). The beam was then reflected from a periscope (mirrors M1/M2), entered a Scanning Galvo head (SGLV) (GSI Lumonics) and was finally focused on the sample surface with a 100 mm given focal length f–θ lens AR coated for 780 nm. Transmission through the scan head (mirrors and lenses) was measured to be >97%. However, above 150 μJ pulse energy, the transmission dropped slightly, probably due to multiphoton absorption in the lens elements. Hence, pulse energies ≤150 μJ were normally used to avoid nonlinear effects which might damage the f–θ lens system. Scan patterns were software generated (SCAPS GmbH). The flat field region is approximately 70×70 mm^2. The spot size $2w_0(1/e^2)$ diameter at the focal plane was estimated to be ∼30 μm from observed single pulse ablation craters (plot of D^2 versus $\ln(E_p)$).

The nominal percentage composition of C263 (Nimonic) is given in Table 1. First row corresponds to values quoted from Ref. [17], while in the second row values from an EDX analysis of the samples used in the present study is reported. The large sheet of the material (thickness = 2.5 mm) was cut into square pieces of 15×15 mm^2. Their surfaces (initial roughness average $(R_a) = 800 \pm 70$ nm and RMS roughness $(R_q) = 1 \pm 0.10$ μm) were mechanically polished first by using SiC grinding paper (360–4000 grit) and finally by using diamond paste (1–0.04 μm). The samples were cleaned in methanol prior to laser irradiation. The sample was positioned below the f–θ lens, on an Aerotech moving stage which could be moved in the x, y and z directions with accuracy of ±0.5 μm.

Laser machined features on the sample surface were imaged by Scanning Electron Microscopy (SEM) using a Hitachi S-2460N instrument as well as by white light scanning interferometric microscopy using a Wyko NT1100 instrument. For a detailed 3D high resolution characterisation of single pulse laser ablated craters, Atomic Force Microscopy (AFM) imaging was also performed using a Veeco CP-II instrument in contact mode with Si cantilevers (Tap300). The laser beam was scanned in a circle (diameter: 3.1 mm) around a carbon coated grid (diameter: 3 mm), and in this way the debris produced during material laser ablation was collected onto the grid for Transmission Electron Microscopy (TEM) studies. TEM was performed with a JEOL JEM-3010 instrument equipped with EDS Genesis 4000 system to enable also acquisition of EDX spectra. For EDX analysis of the bulk material, using the TEM, the sample was mechanically polished down to a thickness of ∼150 μm, a "disk" with diameter of 3 mm was cut, which was subsequently thinned to a thickness of ∼100 nm using ion milling.

3 Results and discussion

3.1 Ablation threshold and dependence on number of laser pulses-incubation effect

The single pulse ablation threshold of the superalloy which represents the minimum laser fluence required to initiate ab-

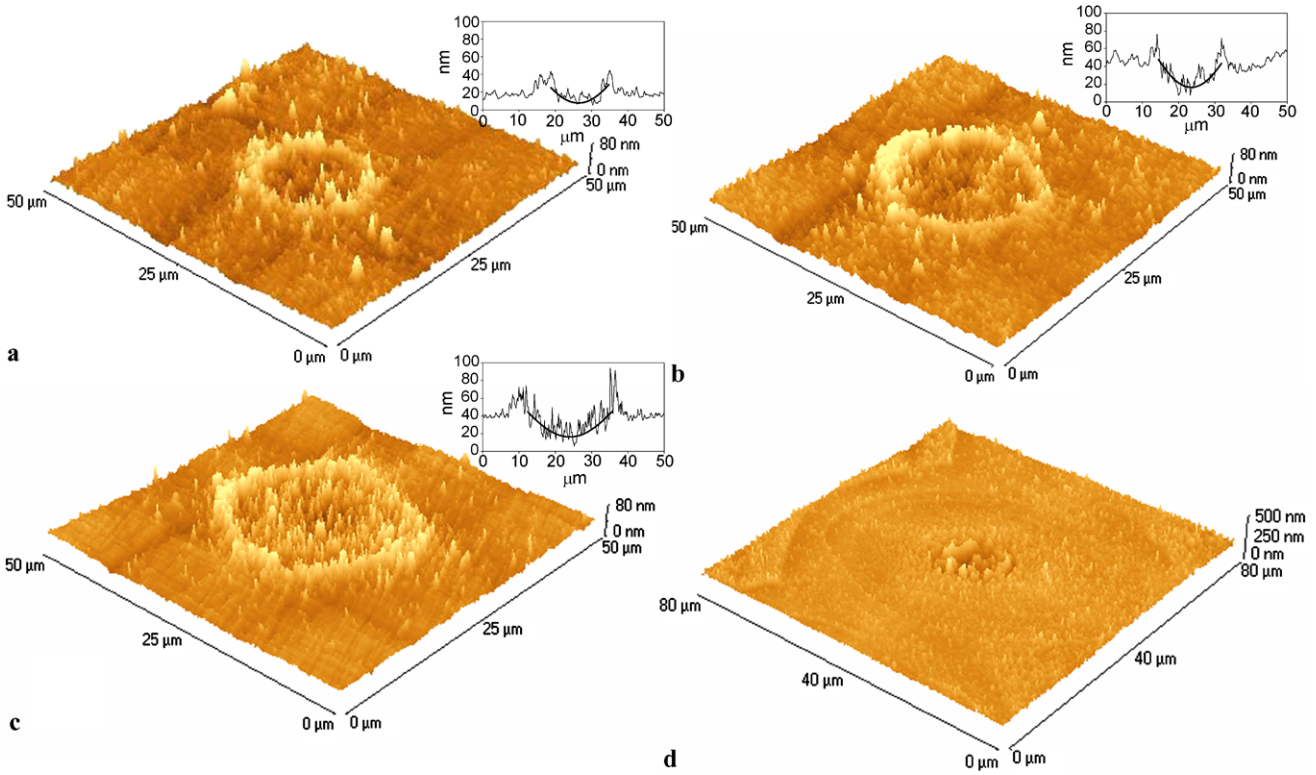

Fig. 2 AFM images of single pulse ablated craters using fluences of: 0.39 **a**, 0.65 **b**, 0.91 **c** and 36.95 **d** J/cm^2, respectively

lation with the first laser pulse was determined by ablating a series of craters on the sample surface with different pulse energies. To obtain craters corresponding to single pulses, the beam was scanned along a line pattern but with speed ≥60 mm/s. In this way by taking into account the pulse length (180 fs) and pulse frequency of 1 kHz, a series of craters with centre to centre distances between them of ∼60 μm along the line length was obtained, which were isolated from each other considering that the beam diameter at the focal point of the f–θ lens is ∼30 μm. Typical AFM images of single pulse ablated craters for low fluences in the region of 0.3–1 J/cm^2 are shown in Fig. 2. In the same figure a single pulse ablated crater using high fluences (36.95 J/cm^2) is also shown. The surface morphology of the craters will be discussed later in Sect. 3.3 of the paper. The ablation threshold was determined by following the well-known method in determining materials laser ablation thresholds [18, 19]. This method predicts that for a Gaussian spatial beam fluence profile with a $1/e^2$ laser beam radius w_0:

$$F(r) = F_0^{\mathrm{pk}} \exp\left(-\frac{2r^2}{w_0^2}\right), \tag{1}$$

where F_0^{pk} is the peak laser fluence (the fluence at the centre for $r = 0$), the laser ablated crater square diameter is given by the relation

$$D^2 = 2w_0^2 \ln\left(\frac{F_0^{\mathrm{pk}}}{F_{\mathrm{th}}}\right) = 2w_0^2 \ln\left(\frac{E_{\mathrm{p}}}{E_{\mathrm{th}}}\right), \tag{2}$$

where E_{p} is the pulse energy related to F_0^{pk} with the relation

$$F_0^{\mathrm{pk}} = \left(\frac{2E_{\mathrm{p}}}{\pi w_0^2}\right), \tag{3}$$

because E_{p} is the integrated value of the Gaussian fluence profile over infinite radius (i.e. from $r = 0$ to ∞). From the AFM as well as from interferometric microscopy images of the craters, the diameters of at least ten craters for the same pulse energy were measured along at least four different directions for the same crater in order to average out the statistical errors in the measured crater diameter. First the square crater diameters (D^2) were plotted versus $\ln(E_{\mathrm{p}})$ and from the slope of the least square fitted line to the data points, the precise beam radius $w_0 = 15.7 \pm 0.2$ μm at the interaction surface was determined (according to (2)), which is needed in order to estimate precisely the peak fluence F_0^{pk} (according to (3)). Because the measured Gaussian spot size on the surface is not necessarily equal to the calculated spot size at the focal point of the f–θ lens, this technique provides a convenient way in determining the exact Gaussian beam spot size at the interaction surface. Then, D^2 was plotted versus $\ln(F_0^{\mathrm{pk}})$ and by taking into account the estimated w_0, the extrapolation of the linear fit (according to (2)) to

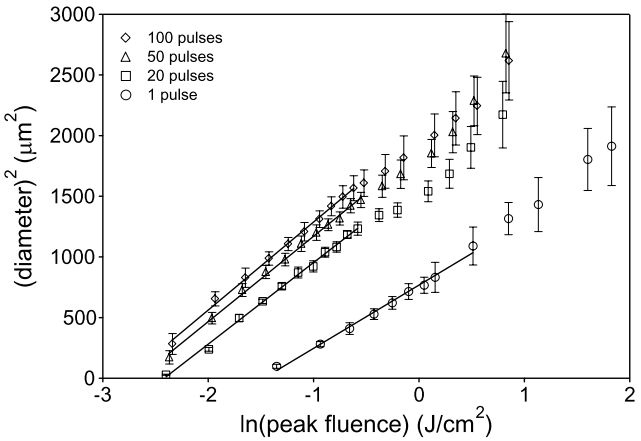

Fig. 3 Plot of the square of crater diameters versus logarithm of fluence, from which the ablation thresholds for different pulses were determined

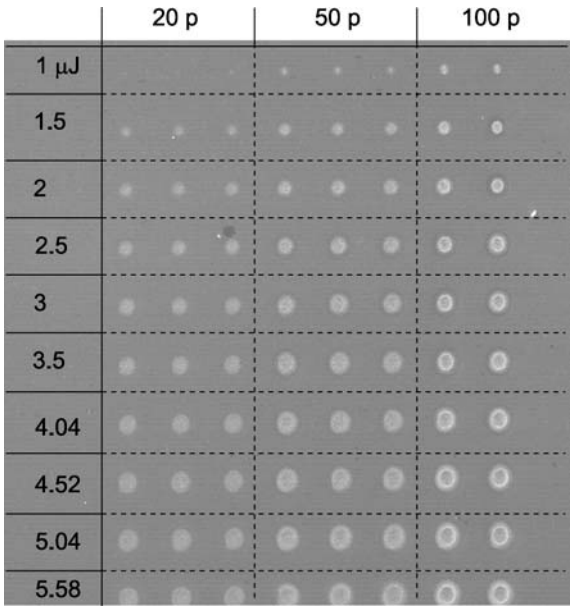

Fig. 4 SEM image of an array of craters (dimples) ablated on the surface of C263 with different pulses (20, 50 and 100) and different pulse energies (1–5.58 μJ)

$D^2 = 0$ results in the determination of the single pulse ablation threshold: $F_{\text{th}}^1 = 0.26 \pm 0.03$ J/cm^2 (circle points in the graph of Fig. 3). The error bars represent the $\pm\sigma$ values (σ: standard deviation of the statistical distribution of the diameter measured values).

Next the incubation effect, (i.e. the dependence of ablation threshold on the number of laser pulses) was investigated on the superalloy C263 by measuring the diameters of multipulse ablated craters (number of pulses $N = 20$, 50 and 100) for different fluences. The incubation effect in metals is known to be due to the formation of a thermally induced plastic stress-strain in the material due to the accumulation of energy from the laser radiation because of its

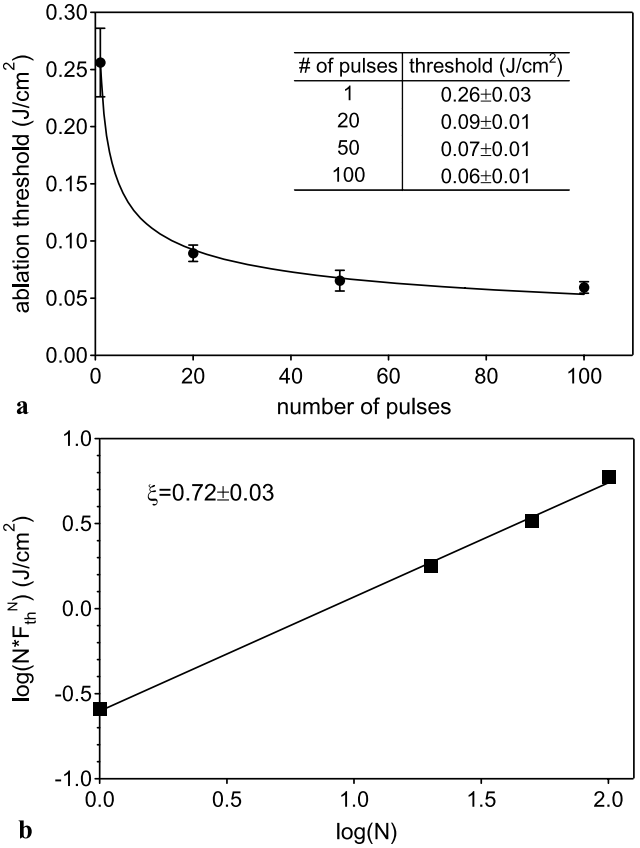

Fig. 5 Ablation thresholds versus number of pulses **a** and $\log(N * F_{\text{th}}^N)$ versus $\log(N)$ **b**

not complete dissipation (during the repetitive pulse irradiation). This stress-strain in turn results in a local plastic deformation of the material providing that the yield strength of the surface is exceeded during each pulse [20, 21]. Such a cumulative effect may also generate surface defects and deteriorate the surface quality of the material which can lead to ablation at a lower threshold. For a simple comparison of the magnitude of change of multipulse ablated crater sizes using different pulse energies, in Fig. 4 an SEM image is shown which includes within the field of view craters ablated with different number of pulses as well as using different pulse energies (higher magnification of each crater individually is shown in Fig. 7, which will be discussed later in Sect. 3.3 of the paper). The ablation threshold corresponding to each number of pulses was determined following the same procedure as for the determination of the single pulse ablation threshold outlined above. From the graph of Fig. 3 it is seen that a linear relationship between the square of the crater diameter (D^2) and the logarithm of the laser fluence ($\ln(F_0^{\text{pk}})$) described by (2), is valid also in the case of multipulse ablated craters. The resulting ablation thresholds versus number of pulses are plotted in Fig. 5a (the values of the ablation thresholds versus number of pulses are summarised in the inset table of Fig. 5a). It is readily seen that the ablation

threshold decreases with the number of pulses. The most dramatic decrease of the ablation threshold is observed during the first 20 laser pulses: the single pulse ablation threshold of 0.26 J/cm^2 is reduced to 0.09 J/cm^2 when 20 laser pulses are applied, which is an almost 65% decrease. As the number of pulses increases beyond 20, the percentage of decrease of the ablation threshold with number of pulses becomes lower: from 0.09 to 0.06 J/cm^2, an almost ∼34% decrease for an increase of the number of pulses from 20 to 100. Thus it is seen that the threshold fluence tends asymptotically to a constant value F_{th}^{∞} (equal to about 0.05 J/cm^2 in this case) as the number of pulses $N \to \infty$. In physical terms this means that irradiation at a fluence F below that level, $F < F_{\text{th}}^{\infty}$, would require an infinite number of pulses to initiate macroscopic damage. The change of the multi-pulse ablation threshold with the number of pulses (shown in Fig. 5a) is described mathematically by the so-called incubation model [22]. This is an empirical model which is based on the assumption that the change of the ablation threshold between the Nth pulse and a pulse previous to that is proportional to the threshold at that pulse. With this assumption, the behaviour of the change of the threshold with the number of pulses which is observed experimentally is described mathematically quite well, i.e. the change of the ablation threshold with the number of pulses due to the incubation is very large for the first few pulses and then slows down for subsequent laser pulses until it reaches an almost constant level for a high number of laser pulses. The degree of incubation is described by the so-called incubation factor ξ, which is a fitting parameter used to describe the decrease in the measured ablation threshold observed when multiple laser pulses are incident on the same surface area. ξ is determined by the relation

$$F_{\text{th}}^{N} = F_{\text{th}}^{1} N^{\xi - 1} \tag{4}$$

by plotting the $\log(N F_{\text{th}}^{N})$ versus $\log(N)$ (Fig. 5b). From the slope of the linear fit ($\chi^2 = 0.00215$) it was found that $\xi = 0.72 \pm 0.03$ for the superalloy C263. The curve in the graph of Fig. 5a corresponds to a plot of the above relation with $F_{\text{th}}^{1} = 0.26$ and $\xi = 0.72$.

3.2 Ablation rate and dependence on laser fluence-ablation mechanisms

The depths of single pulse as well as of 100 pulses ablated craters, were measured with the AFM. For comparison, the images in Fig. 2 of single pulse ablated craters at low fluences have been rescaled identically along the z-axis (0–80 nm z-scale range). Typical cross sectional graphs taken along the crater centres are shown at the right-hand side of each image. Due to the specific surface morphology of the ablated craters of the material, especially at low fluences where the ablation depth is very small, the cross sections do not appear as "smooth" curves with a well-defined

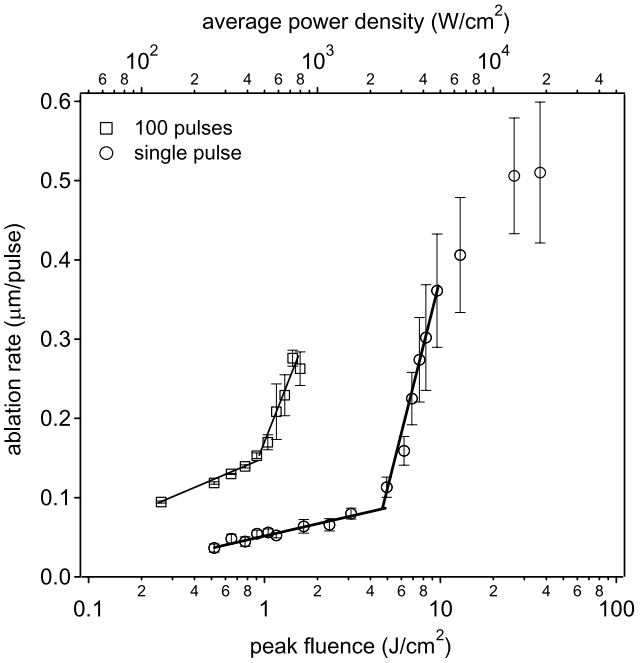

Fig. 6 Ablation rate versus logarithm of peak fluence (*bottom scale*) and average power density (*top scale*) for single pulse (*circle points*) and 100 pulses (*square points*), ablated craters

point of maximum depth but they rather exhibit sharp peaks and valleys fluctuating around a certain ablation profile. Thus the depths of the craters were determined by fitting to the ablation cross sections a Gaussian curve (in a simple first approximation) and taking the point of minimum of that curve as the depth of the crater. The solid lines in the graphs in Fig. 2a–c demonstrate this method. The graph of the measured ablation depths versus the logarithm of fluence (Fig. 6) for the superalloy C263 (like in the case of the superalloy CMSX-4 [14] as well as for a number of other materials ranging from polymers to semiconductors [23] and metals [24]) shows two different dependencies of depth on fluence corresponding to the two ablation regimes dominated either by the optical penetration depth of the radiation or the electron thermal diffusion length. Fitting to the experimental data points in the low fluences regime ($F_{\alpha} = 0.52$–3.10 J/cm^2) the relation

$$d_{\alpha} = \alpha^{-1} \ln\left(\frac{F_{\alpha}}{F_{\text{th}}^{\alpha}}\right), \tag{5}$$

which describes the ablation rate (d_{α}) [22, 25, 26] in this regime according to the two temperature model [26], provides values for the optical penetration depth (neglecting the electron heat conduction term in the diffusion equations) of $\alpha^{-1} = 37.2$ nm and for the threshold corresponding to this region of $F_{\text{th}}^{\alpha} = 0.24$ J/cm^2. The value for F_{th}^{α} agrees very well with the value of the single pulse ablation threshold which was determined previously in Sect. 3.1 using mea-

surements of the single pulse crater diameters versus fluence, and it is the minimum fluence to produce a single pulse crater on the material surface. In this regime the density of hot-electrons is so low that the energy penetration depth is controlled by the optical absorption length, and the ablation rate is dominated by the optical penetration depth of the laser radiation into the material. The value 37.2 nm obtained for the optical penetration depth is larger than the corresponding value for Ni (∼15 nm) [27] as well as for CMSX-4 (18 nm) [14]. This might be due to the fact that the superalloy C263 contains lower percentage of Ni (∼50%) as compared to the CMSX-4 (61.7%). The second ablation regime for the superalloy C263 is observed for fluences greater than ∼5 J/cm^2 (corresponding to the change of slope of the curve in Fig. 6), exhibiting a large increase of the ablation rate (d_ℓ) with laser fluence (F_ℓ). Fitting to the experimental data points in this regime ($F_\ell = 4.96$–8.28 J/cm^2) the relation [22, 25]

$$d_\ell = \ell \ln\left(\frac{F_\ell}{F_{\text{th}}^\ell}\right) \tag{6}$$

provides values for the energy penetration depth ("electron heat diffusion length," which characterises the length over which the heat has been carried out by the electrons) $\ell \approx 387$ nm and for the threshold corresponding to this region $F_{\text{th}}^\ell = 3.84$ J/cm^2. This value is lower than the value of ∼5 J/cm^2 (where the change of slope of the curve in Fig. 6 is observed) because it corresponds to the intersection of the extrapolation of the data-fitting line in the high fluences region with the horizontal axis. F_{th}^ℓ is the minimum fluence beyond which the electron temperature which becomes maximum at the material surface is sufficiently high to sustain carrier diffusion in the bulk of the material. At high fluences (>30 J/cm^2) the ablation rate tends to a saturation with laser fluence. This is not due to plasma shielding and screening effects (partial absorption of the laser radiation by the expanding plasma) because of the ultrashort pulses which we consider here in combination to the pulse frequency but it might be rather due to the fact that as the crater depth increases with fluence, at a certain depth the characteristic time during which the melt attains the critical velocity for ejection becomes longer than the time it takes for the melt to cool down and resolidified according to the so called "piston model" [28]. In the same graph of Fig. 6 (square points) the ablation rate corresponding to 100 pulses determined by measuring the depths of craters ablated with 100 pulses and dividing by 100 is also shown. Straight line fitting in the region of fluences (0.26–0.91 J/cm^2) yields $F_{\text{th}(100)}^\alpha = 0.05$ J/cm^2 very close to the 100 pulses ablation threshold ($F_{\text{th}}^{100} = 0.06$ J/cm^2) determined previously in Sect. 3.1 (Figs. 3 and 5a).

3.3 Surface morphology of ablated craters-evolution with laser fluence and number of pulses

Around the perimeter of single pulse ablated craters (dimples) even in the low fluence region (<5 J/cm^2 (Figs. 2a–c) where the ablation is dominated by the optical penetration depth, a rim of material (burr) which is raised by ∼10–20 nm above the sample surface is observed. This rim corresponds to resolidified splash of a molten material layer generated during the ablation process (recast material), and it has also been observed during femtosecond laser ablation of usually transition metals (Co, Cr, Mo, W, Fe) [29, 30] but it is absent in the case of femtosecond laser ablation of noble metals (Cu, Au) [31] due to the fact that in the case of transition metals the transfer of energy from the electrons to the lattice proceeds much faster because of the strongest electron-phonon coupling. Such a rim of molten material has not been observed in the case of single pulse ablation craters of the superalloy CMSX-4 at similar fluences [14] nor in the case of microprocessing of the superalloy MK-4 [12] due possibly to the lower "electron heat diffusion length" in these alloys because of the lower percentage of Co, Cr, Mo and the absence of Fe (d-block elements with higher number of valence electrons than Ta and W) in those materials as compared to the superalloy C263. This in turn indicates that it is more difficult to femtosecond laser micromachine the superalloy C263 as compared to CMSX-4 or MK-4, since thermal effects start becoming significant even at low fluences. By considering the following set of parameters for the superalloy C263: density $\rho = 8.38$ g/cm^3 [17] and heat capacity $C_P = 577$ J kg^{-1} K^{-1} calculated at an average temperature of $T = 963$ K (between room temperature $T_0 = 298$ K and the melting temperature of the superalloy $T_{\text{m}} = 1628$ K) for its given 0.45% Al alloy composition [32], the rise of temperature of a layer of the material with thickness d_{abs} equal to the laser optical energy penetration depth of $\alpha^{-1} = 37.2$ nm (measured in Sect. 3.2 of the paper) for a fluence of $F = 0.039$ J/cm^2 (assuming that only 10% of the incidence energy fluence of 0.39 J/cm^2 remains in the material as thermal energy, the rest 80% is used by the expanding plasma to move the ambient air with a small part lost in radiation), is $\Delta T = F/(\rho C_P d_{abs}) \approx 2160$ K, i.e. above the superalloy melting temperature. Thermocapillary forces induced by the temperature gradient on the surface (which in turn creates surface tension gradients) because of the Gaussian beam profile of the laser beam (the surface liquid is not heated uniformly), as well as hydrodynamic forces due to pressure gradients caused by the plasma that is formed above the molten layer (these gradients are particularly large at the edges of the ablated crater because of the plasma/air interface), are exerted on the molten fluid layer, moving it from the centre of the crater to the edge and thus depositing a thin rim around the ablated area. In the high

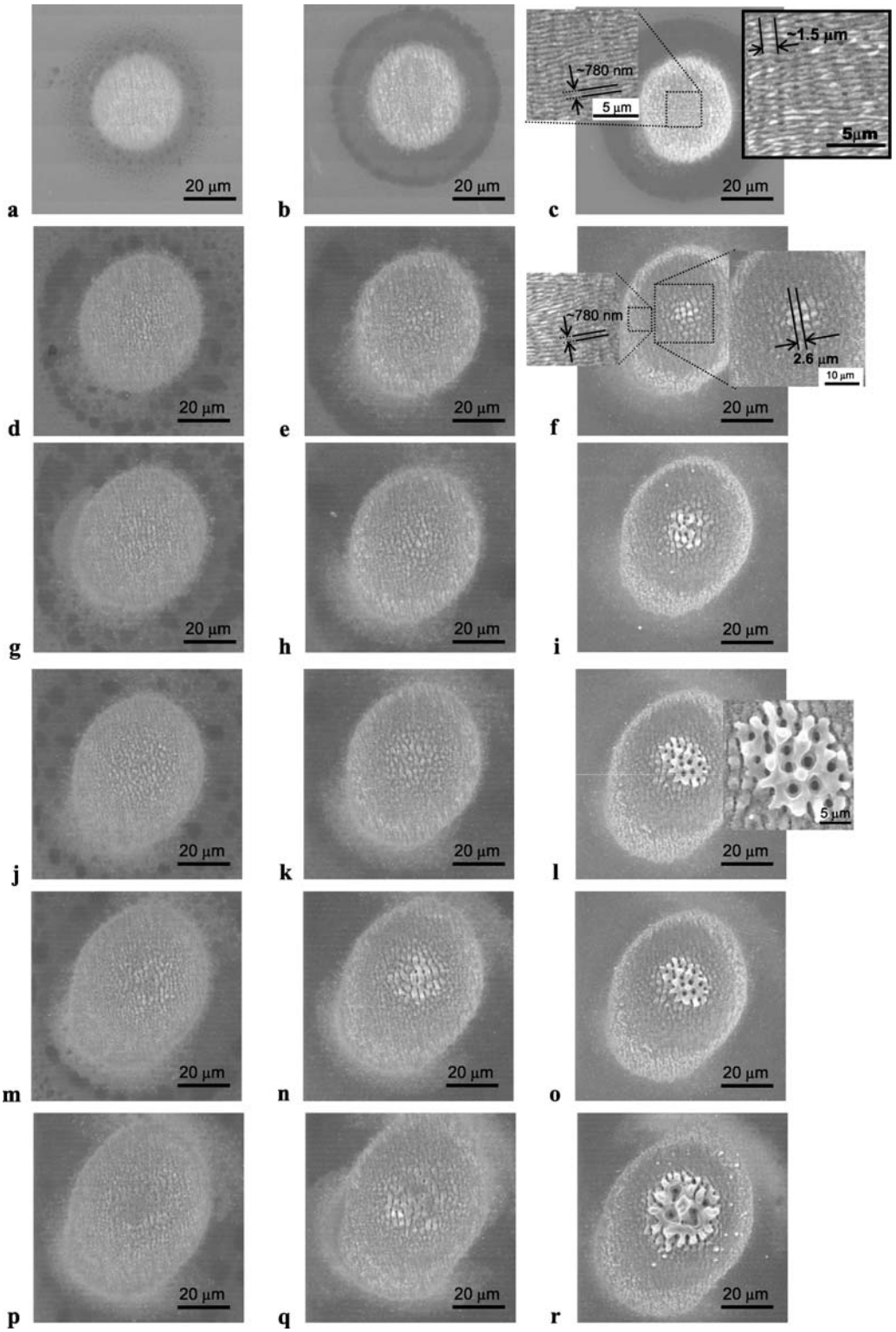

Fig. 7 SEM images of craters (dimples) ablated on the superalloy C263 with 20 pulses and fluences of: 0.27 **a**, 0.81 **d**, 1.09 **g**, 1.34 **j**, 1.64 **m** and 2.21 **p** J/cm^2, 50 pulses and fluences of: 0.28 **b**, 0.84 **e**, 1.13 **h**, 1.38 **k**, 1.69 **n** and 2.28 **q** and 100 pulses and fluences of: 0.29 **c**, 0.87 **f**, 1.16 **i**, 1.41 **l**, 1.74 **o** and 2.35 **r** J/cm^2, respectively. The right–hand side image in **c** corresponds to $F = 0.14$ J/cm^2 (100 pulses)

fluences region ($F > 5$ J/cm^2) where ablation is dominated by the electron thermal diffusion length as it was analysed in Sect. 3.2, melting and resolidification of material is observed in the inner central region of the ablated crater (Fig. 2d).

Figure 7 shows the evolution with laser fluence of the surface morphology of craters ablated with 20, 50 and 100 pulses. For low fluences ($F < 0.44$ J/cm^2), the surface morphology of the ablated craters in the whole crater surface area is characterised by ripples (this is shown clearly, for instance in the left-hand side higher magnification inset image in Fig. 7c, $F = 0.29$ J/cm^2). These appear as periodic surface structures with period of ∼780 nm very close to the wavelength of the laser radiation (775 nm) and orientation perpendicular to the polarisation direction of the laser light in agreement with the classical model for their formation for normal incidence of the laser radiation on the sample surface in ambient air [33]. These periodic structures are well known to be formed in almost every material, from metals [21] to semiconductors [34, 36] and dielectrics [35] as a result of the laser irradiation with low fluences where the thermal effects are negligible. Several models have been proposed to explain their formation including interference between the incident laser beam and an optical wave travelling very close to the surface of the sample (polariton) caused by the scattering of the incident laser light by the disturbances of the height of the sample surface (roughness or grain boundaries) or by nonuniform temperature and/or electron density which results in material ablation along the lines of constructive interference [33]. According to this model, the ripples which are created at the beginning during the first few pulses provide a sinusoidal corrugation which acts as a grating for subsequent ripple growth. Holes (pits) with average diameter of ∼300–400 nm also appear inside the channels between the ripples. These holes for very low fluences ($F = 0.14$ J/cm^2 for 100 pulses, right-hand side image in Fig. 7c) are lying along lines which are directed almost perpendicular to the ripples with the average distance between the lines ∼1.5 μm and somehow interrupt the ripple continuation. As the fluence increases, the size of those pits increases, and eventually they join together forming channels (Fig. 7f and right-hand side inset). However at very high fluences, formation of these channels at higher number of pulses follows an initial flat surface melting at lower number of pulses, as it is seen in Fig. 7p, $F = 2.21$ J/cm^2 (20 pulses) and Fig. 7q, $F = 2.28$ J/cm^2 (50 pulses). For the same number of pulses, the fluence above which the channels start to be formed at the centre of the ablated crater is higher the lower the number or pulses. This can be observed by following the SEM images of Fig. 7 for the same number of pulses and for increasing fluence. The channels and the areas between them form another lower frequency periodic structure, at the centre of the ablated craters, now characterised by higher periodicity (period ∼2.6 μm) (right-hand side inset in Fig. 7f). Outside of this area the higher spatial frequency ripples (period ∼780 nm) still appear (left-hand side inset in Fig. 7f). It is interesting to note that the fluence at which the low frequency periodic structures start appearing at the centre of the ablated craters (for instance ∼0.87 J/cm^2 for the 100 pulses ablated craters (Fig. 7f)) agrees well with fluences which lie just below the "critical" fluence at which the change of slope of the 100 pulses ablation rate versus fluence curve is observed (∼0.9 J/cm^2, square points in the graph of Fig. 6), while the higher fluences where this central periodic structure degenerates to a melted and resolidified region ($F \geq 1.16$ J/cm^2, Fig. 7i, l, o and r) lie in the high fluences region of the curve where ablation is dominated by the electron thermal diffusion length. Periodic structures with spatial frequency lower than the frequency of the periodic structures corresponding to the wavelength of the laser light have also been observed previously on craters ablated with multipulse femtosecond irradiation but on III–V semiconductors, Si, Ge and diamond crystals ([36] and references therein). Observation of these structures here mark the onset for the appearance of thermal effects at the centre of the ablated craters. For the 100 pulses ablation as the fluence increases beyond the fluence for the formation of the low frequency central periodic structures, flat surface melting is not observed, but the structures rather degenerate to irregular shape structures at the centre of the ablated crater characterised by holes with average diameters of ∼1.3–1.7 μm (Fig. 7l, o and r). The creation of these holes may be explained by the burst of air bubbles which are formed inside the boiling liquid, accompanied by rapid cooling and resolidification of the material.

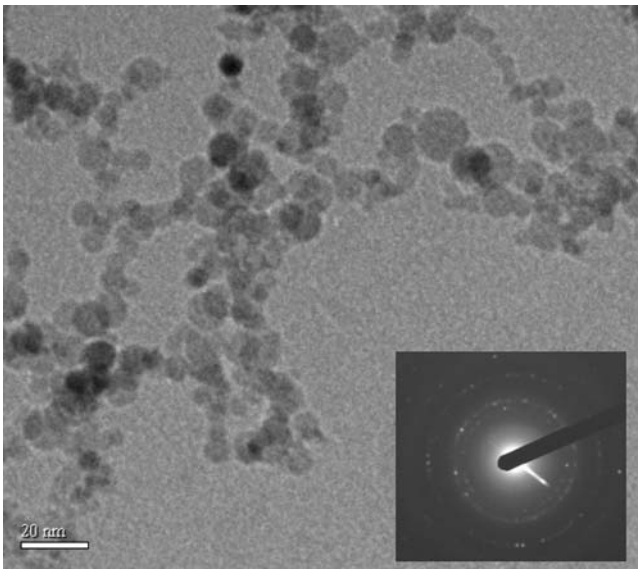

Fig. 8 TEM image showing nanoparticles of C263 formed by the debris produced by femtosecond laser ablation of the material. *Inset* shows selected area e^--diffraction pattern of the nanoparticles

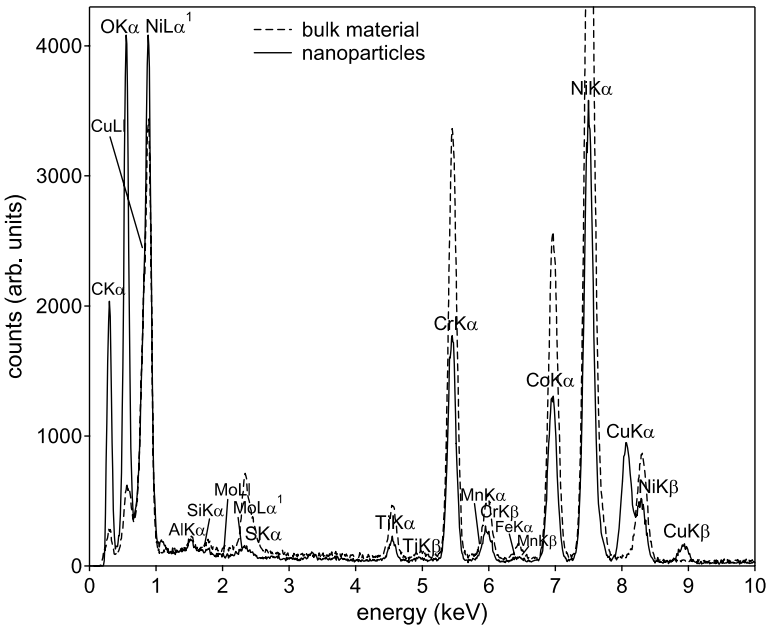

Fig. 9 EDX spectrum of C263 nanoparticles (*solid line*) and of the bulk material (*dashed line*)

Table 2 Elemental composition (%wt) of superalloy C263 nanoparticles

O	C	Si	Cu	Fe	Mn	Cr	Ti	Al	Co	Mo	Zr	B	S	Ni
20.6	–	0.2	–	0.4	0.5	16.7	1.2	0.3	15.3	2.4	0.3	0.0	0.9	41.5
–	–	0.2	–	0.5	0.5	21.0	1.6	0.3	19.2	3.9	0.4	0.0	0.9	51.5

3.4 Analysis of the debris produced during ablation

TEM images of the debris which is produced by laser ablation of the alloy (Fig. 8) show that it consists of nanoparticles with diameters of ∼2–20 nm (for nanoparticles created by ablating the target material using ∼9.6 J/cm^2). The selected area electron diffraction pattern (inset in Fig. 8) shows that the nanoparticles have crystalline structure. EDX spectra shown in Fig. 9 of the nanoparticles (solid line) and of the bulk material (dashed line) and their corresponding elemental compositions (%wt) (shown in Table 2) confirm that the produced nanoparticles contain all elements of the target material and also with comparable stoichiometry (the two rows in Table 2 correspond to taking or not into account in the peak analysis, the peak corresponding to oxygen). These findings establish a direct correlation between the bulk material C263 and the debris nanoparticles which are produced as a result of the femtosecond laser microprocessing of the material, in terms of structure and elemental composition. In addition the presence of the strong oxygen peak in the EDX spectra for the nanoparticles also indicates that the produced nanoparticles have been oxidised possibly due to the interaction of the plasma plume with air molecules (ablation done in ambient air). Nanoparticles in general are important nanomaterials for a number of applications in different scientific fields, and femtosecond laser ablation seems an alternative method for their synthesis. Furthermore since the high concentration of ferromagnetic elements of Ni, Co and Cr of the target material is also retained in the produced nanoparticles, the nanoparticles of C263 produced here by femtosecond laser ablation of the target material can be used as nanomagnets in a range of different applications in engineering or biological fields.

4 Conclusions

Femtosecond laser ablation characteristics and mechanisms of the nickel based superalloy C263 have been investigated and correlated with the properties of the material. The single pulse ablation threshold is determined to be $F_{\mathrm{th}}^{1} = 0.26 \pm 0.03\mathrm{J/cm}^2$ and the incubation parameter $\xi = 0.72 \pm 0.03$. A ∼65% decrease of the ablation threshold to 0.09 J/cm^2 is obtained when 20 pulses are used to ablate the material. The ablation mechanism changes from optical penetration depth to the one determined by the electron thermal diffusion length at ∼5 J/cm^2 (for single pulse ablation) and the parameters for the two regimes of ablation were determined: at low fluences ($F = 0.5$–4 J/cm^2), $\alpha^{-1} = 37.2$ nm, $F_{\mathrm{th}}^{\alpha} = 0.24$ J/cm^2 and at high fluences ($F = 5$–9 J/cm^2), $\ell \approx 387$ nm, $F_{\mathrm{th}}^{\ell} = 3.84$ J/cm^2. Different parameters of ablation rate dependence on fluence were obtained for multi-

pulse ablation. The debris consists of C263 oxidised crystalline nanoparticles. For low fluences, the central surface morphology of multipulse ablated craters (dimples) is characterised by ripples which exhibit the laser wavelength periodicity, while at high fluences melting and resolidification is observed.

Acknowledgements N.G.S. acknowledges support by a Marie Curie Fellowship of the European Community, Grant Number MTKD-CT-2004-517165. This work was carried out with the assistance of the North West Laser Engineering Consortium (www.nwlec.org.uk) a project funded by the North West Development Agency (NWDA) in the U.K.

References

1. X. Chen, W. Lotshaw, A.L. Ortiz, P.R. Staver, C.E. Erikson, M.H. McLaughlin, T.J. Rockstroh, J. Laser Appl. **8**, 233 (1996)
2. N. Syred, A. Khalatov, A. Kozlov, A. Shchukin, R. Agachev, J. Turbomach. **123**, 609 (2001)
3. K. Kanokjaruvijit, R.F. Martinez-Botas, Int. J. Heat Mass Transf. **48**, 161 (2005)
4. H. Schilchting, K. Gersten, *Boundary-Layer Theory*, 8th edn. (Springer, Berlin, 2001)
5. X. Wang, J.Y. Zhu, W. Chen, L. Cai, Int. J. Comput. Appl. Technol. **29**, 114 (2007)
6. D. Pantelis, P. Psyllaki, Mater. Manuf. Process. **11**, 271 (1996)
7. M.J. Cronin, Proc SPIE—Int. Soc. Opt. Eng. 469 (1993)
8. S. Bandyopandhyay, J.K. Sarin-Sundar, G. Sundararajan, S.V. Joshi, J. Mater. Process. Technol. **127**, 83 (2002)
9. X. Liu, D. Du, G. Mourou, IEEE J. Quant. Electron. **33**, 1706 (1997)
10. Clark-MXR Inc., Laser ablation and micromachining with ultrashort laser pulses. http://www.cmxr.com/
11. B.N. Chichkov, C. Momma, S. Nolte, V. von Alvensleben, A. Tünnermann, Appl. Phys. A **63**, 109 (1996)
12. Q. Feng, Y.N. Picard, H. Liu, S.M. Yalisove, G. Mourou, T.M. Pollock, Scr. Mater. **53**, 511 (2005)
13. Q. Feng, Y.N. Picard, J.P. McDonald, P.A. van Rompay, S.M. Yalisove, T.M. Pollock, Mater. Sci. Eng. A **430**, 203 (2006)
14. S. Ma, J.P. McDonald, B. Tryon, S.M. Yalisove, T.M. Pollock, Metall. Mater. Trans. A **38**, 2349 (2007)
15. Q. Wen, Q. Feng, G. Cheng, W. Zhao, Z. Sun, Mater. Sci. Forum **546**, 1309 (2007)
16. D. Strickland, G. Mourou, Opt. Commun. **56**, 219 (1985)
17. W. Betteridge, J. Heslop, *The Nimonic Alloys* (Edward Arnold, Sevenoaks, 1974)
18. J. Bonse, J.M. Wrobel, J. Krüger, W. Kautek, Appl. Phys. A **72**, 89 (2001)
19. J.M. Liu, Opt. Lett. **7**, 196 (1982)
20. C.S. Lee, N. Koumvakalis, M. Bass, Appl. Phys. Lett. **41**, 625 (1982)
21. Y. Jee, M.F. Becker, R.M. Walser, J. Opt. Soc. Am. B **5**, 648 (1988)
22. C. Momma, S. Nolte, B.N. Chichkov, F.V. Alvensleben, A. Tunnermann, Appl. Surf. Sci. **109/110**, 15 (1997)
23. D.J. Hwang, C.P. Grigoropoulos, T.Y. Choi, J. Appl. Phys. **99**, 083101 (2006)
24. C. Momma, B.N. Chichkov, S. Nolte, F. von Albenleben, A. Tunnermann, H. Welling, Opt. Commun. **129**, 134 (1996)
25. S. Nolte, C. Momma, H. Jacobs, A. Tünnermann, B.N. Chichkov, B. Wellegehausen, H. Welling, J. Opt. Soc. Am. B **14**, 2716 (1997)
26. S.I. Anisimov, M.I. Tribel'ski, Ya.G. Epel'baum, Sov. Phys. JETP **51**, 802 (1980)
27. D.R. Lide, *CRC Handbook of Chemistry and Physics*, 71st edn. (CRC Press, Boca Raton, 1990)
28. A. Ruf, D. Breitling, P. Berger, F. Dausinger, H. Hügel, SPIE **4830**, 73 (2003)
29. F. Korte, J. Serbin, J. Koch, A. Egbert, C. Fallnich, A. Ostendorf, B.N. Chichkov, Appl. Phys. A **77**, 229 (2003)
30. F. Dausinger, RIKEN Rev. **50**, 77 (2003) (LPM 2002)
31. S.S. Wellershoff, J. Hohlfeld, J. Güdde, E. Matthias, Appl. Phys. A **69**, S99 (1999)
32. K.C. Mills, Y.M. Youssef, Z. Li, Y. Su, ISIJ Int. **46**, 623 (2006)
33. Z. Guosheng, P.M. Fauchet, A.E. Siegman, Phys. Rev. B **26**, 5366 (1982)
34. J. Bonse, J.M. Wrobel, J. Krüger, W. Kautek, Appl. Phys. A **72**, 89 (2001)
35. D. Ashkenasi, A. Rosenfeld, H. Varel, M. Wahmer, E.E.B. Campbell, Appl. Surf. Sci. **120**, 65 (1997)
36. A. Borowiec, H.K. Haugen, Appl. Phys. Lett. **82**, 4462 (2003)